AD-A139 900 RADIATION GROWTH IN A MILLIMETER-WAVE FREE-ELECTRON LASER OPERATING IN THE COLLECTIVE REGIME(U) NAVAL RESEARCH LAB WASHINGTON DC S H GOLD ET AL. 20 MAR 84 1/1

UNCLASSIFIED NRL-MR-5297 F/G 20/5 NL

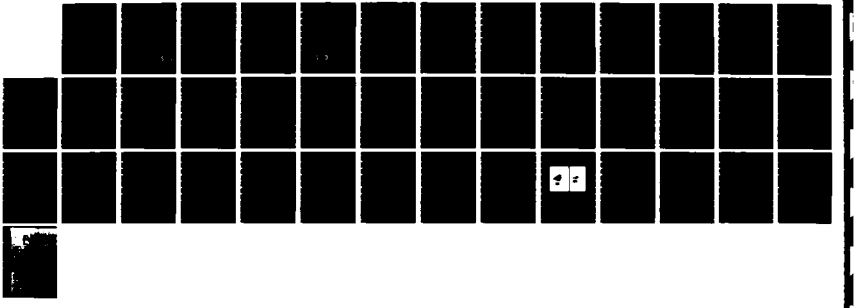

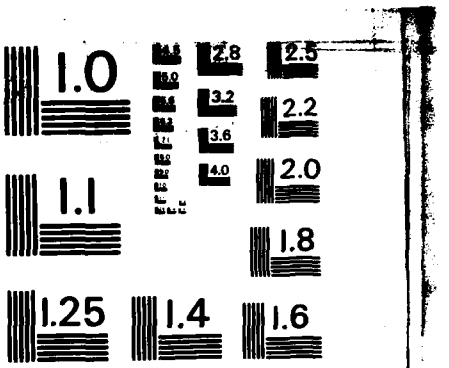

(2)

NRL Memorandum Report 52[illegible]

Radiation Growth in a Millimeter-Wave Free-Electron Laser Operating in the Collective Regime

S. H. GOLD, W. M. BLACK,* H. P. FREUND,**
V. L. GRANATSTEIN,*** AND A. K. KINKEAD

High Power Electromagnetic Radiation Branch
Plasma Physics Division

**George Mason University, Fairfax, VA 22030*

***Science Applications, Inc., McLean, VA 22102*

****University of Maryland, College Park, MD 20742*

March 20, 1984

This research was supported by the Naval Sea Systems Command.

NAVAL RESEARCH LABORATORY
Washington, D.C.

SECURITY CLASSIFICATION OF THIS PAGE

REPORT DOCUMENTATION PAGE

1a. REPORT SECURITY CLASSIFICATION UNCLASSIFIED	1b. RESTRICTIVE MARKINGS
2a. SECURITY CLASSIFICATION AUTHORITY	3. DISTRIBUTION/AVAILABILITY OF REPORT
2b. DECLASSIFICATION/DOWNGRADING SCHEDULE	Approved for public release; distribution unlimited.
4. PERFORMING ORGANIZATION REPORT NUMBER(S) NRL Memorandum Report 5297	5. MONITORING ORGANIZATION REPORT NUMBER(S)
6a. NAME OF PERFORMING ORGANIZATION Naval Research Laboratory 6b. OFFICE SYMBOL (If applicable)	7a. NAME OF MONITORING ORGANIZATION
6c. ADDRESS (City, State and ZIP Code) Washington, DC 20375	7b. ADDRESS (City, State and ZIP Code)
8a. NAME OF FUNDING/SPONSORING ORGANIZATION Naval Sea Systems Command 8b. OFFICE SYMBOL (If applicable)	9. PROCUREMENT INSTRUMENT IDENTIFICATION NUMBER
8c. ADDRESS (City, State and ZIP Code) Washington, DC 20362	10. SOURCE OF FUNDING NOS. PROGRAM ELEMENT NO. 62768N; PROJECT NO.; TASK NO. SF68-342-001; WORK UNIT NO. 47-0920-03
11. TITLE (Include Security Classification) (See page ii)	
12. PERSONAL AUTHOR(S) S.H. Gold, W.M. Black,* H.P. Freund,** V.L. Granatstein,*** and A.K. Kinkead	
13a. TYPE OF REPORT Interim 13b. TIME COVERED FROM _____ TO _____	14. DATE OF REPORT (Yr., Mo., Day) March 20, 1984 15. PAGE COUNT 39
16. SUPPLEMENTARY NOTATION *George Mason University, Fairfax, VA 22030 (Continues) **Science Applications, Inc., McLean, VA 22102 ***University of Maryland, College Park, MD 20742	
17. COSATI CODES FIELD / GROUP / SUB. GR	18. SUBJECT TERMS (Continue on reverse if necessary and identify by block number) Free-electron laser (FEL) Millimeter-wave

19. ABSTRACT (Continue on reverse if necessary and identify by block number)

Frequency-resolved measurements of radiation growth have been performed on a millimeter-wave free-electron laser using an intense relativistic electron beam. These measurements have shown large radiation growth rates (~2 dB/cm) over a broad instantaneous bandwidth (66-90 GHz), in good agreement with predictions of theory for operation in the collective regime. Growth narrowing and saturation effects have also been observed. In addition, a large increase in experimental power and efficiency has been observed to result from tapering the strength of the axial magnetic field in the sense that compensates for kinetic energy extraction from the electron beam. Direct calorimetric measurements indicate the production of ≥ 75 MW centered at 75 GHz with 6% experimental efficiency.

PACS Numbers: 41.70.+t, 52.60.+h, 52.35.Mw, 42.65.Cq

20. DISTRIBUTION/AVAILABILITY OF ABSTRACT UNCLASSIFIED/UNLIMITED ☐ SAME AS RPT. ☒ DTIC USERS ☐	21. ABSTRACT SECURITY CLASSIFICATION UNCLASSIFIED
22a. NAME OF RESPONSIBLE INDIVIDUAL Steven H. Gold	22b. TELEPHONE NUMBER (Include Area Code) (202) 767-3358 22c. OFFICE SYMBOL Code 4740

DD FORM 1473, 83 APR EDITION OF 1 JAN 73 IS OBSOLETE

SECURITY CLASSIFICATION OF THIS PAGE

11. TITLE (Include Security Classification)

RADIATION GROWTH IN A MILLIMETER-WAVE FREE-ELECTRON LASER OPERATING IN THE COLLECTIVE REGIME

16. SUPPLEMENTARY NOTATION (Continued)

This research was supported by the Naval Sea Systems Command under Contract No. SF68-342.

CONTENTS

RADIATION GROWTH IN A MILLIMETER-WAVE FREE-ELECTRON LASER OPERATING IN THE COLLECTIVE REGIME

I. INTRODUCTION

The free-electron laser (FEL), using an intense relativistic electron beam of moderate voltage (1-2 MeV) and low velocity spread ($\Delta\beta_{\parallel}/\beta_{\parallel} \lesssim 0.1\%$) has demonstrated its potential as an extremely high power, moderate efficiency source of continuously tunable radiation in the millimeter-wave range of frequencies. An earlier publication reported a peak power of 50 MW at 75 GHz, corresponding to an efficiency of approximately 5%, from a superradiant free-electron laser operating in the collective regime with a 1 kA, 1.25 MeV electron beam.[1] It also reported the measurement of emission spectra that agreed well with theoretical predictions as well as the tuning of the emission frequency over the range from 60 to 95 GHz. Additionally, a preliminary nonoptimized single-frequency growth rate measurement was performed.

Previous measurements have concentrated primarily on the final output radiation from the FEL, and its scaling (power, frequency, etc.) as a function of experimental parameters. Such a high-power superradiant FEL device has an output power that is many tens of dB larger than the spontaneous emission that initiates the process of radiation growth. Such measurements therefore inevitably contain aspects of starting conditions (spontaneous emission), linear growth, and nonlinear growth/saturation effects that determine the final output power. In this paper, we study in detail the growth of electromagnetic radiation in the superradiant FEL

Manuscript approved January 26, 1984.

experiment. This is done by varying the effective length of the interaction region of the FEL, and observing the effect of this variation on the FEL output radiation. By so doing, one can observe the frequency-resolved growth rate, the spectral shape of the emission as a function of interaction length, and spectral narrowing and saturation effects.

An additional subject of this paper is the study of the effect of placing a taper in the magnitude of the axial magnetic field near the end of the uniform wiggler interaction region. Such an axial field taper results from the method used to vary the effective length of the interaction region of the FEL. Under certain conditions, it is found to strongly affect the emission spectrum, resulting both in an enhancement of the lower frequencies of the FEL emission and in a large overall efficiency enhancement.

II. EXPERIMENTAL APPARATUS

The experimental configuration is shown in Fig. 1. A 1.25 MeV (γ = 3.4), 1 kA, 6-mm-diameter solid electron beam interacts with a transverse wiggler or pump magnetic field while passing through a 10.8 mm i.d. stainless steel drift tube. The electron beam is produced using a pulseline accelerator with 50 nsec pulse duration. A special apertured diode[2] is used to produce an electron beam of very low axial velocity spread ($\Delta\beta_{\parallel}/\beta_{\parallel} \lesssim 0.1\%$). An axial magnetic field, variable up to 20 kG, is used both to form and confine the electron beam and to provide gyroresonant enhancement of the effects of the wiggler magnetic field. The wiggler magnet provides a transverse magnetic field of period λ_w=3 cm, which is variable up to 3 kG over a uniform interaction region of 63 cm,

and contains adiabatic transition regions of 21 cm and 15 cm at its input and output ends. Greater experimental detail has been provided elsewhere.[2]

Spontaneous emission at the injection end of the interaction region is highly amplified by the FEL interaction. Following the interaction, the electrons are sent into the drift tube wall and the amplified radiation is transmitted to a large microwave horn from which it is radiated into an anechoic chamber. Small fractions of the emitted radiation are sampled by a pyroelectric detector equipped with a 60 GHz high-pass filter, to monitor total power in the band of interest, and by a millimeter-wave grating spectrometer[3], in order to perform spectrally-resolved measurement. The spectrometer is equipped with three parallel detection channels, each consisting of a W-band horn, a variable waveguide attenuator, and a crystal detector. The frequency settings and insertion losses of the spectrometer were completely calibrated over the range of 60 to 100 GHz using V-band and W-band sweepers. The resolution of the spectrometer is approximately 1 GHz. Each variable attenuator was calibrated as a function of setting and frequency against a precision broadband calibrated attenuator, and each crystal detector was absolutely calibrated over the complete range of frequencies and incident power levels at which it was used during the experiment. In addition, in order to extend the dynamic range of the measurements, a removable calibrated attenuator pad of approximately 20 dB was placed before the spectrometer. The fraction of radiation sampled by the spectrometer was chosen to provide an appropriate signal level from the detector at the highest experimental power levels when the attenuator pad was in place and 10 to 20 dB of attenuation was set on each channels' variable

attenuator. This made possible accurate relative power readings, by changing only the amount of calibrated attenuation in front of each detector, at approximately constant detector signal levels, as the experimental power was reduced over a range exceeding 30 dB in order to measure radiation growth rates.

The effective length of the interaction region is varied by changing the length of the magnet which supplies the axial magnetic field. As will be discussed later, the decreasing axial field near the end region of this solenoidal magnet rapidly sends the electron beam into the drift tube wall, effectively ending the FEL interaction. Thus, by observing the evolution of the emission spectrum as incremental changes are made in the length of the solenoidal magnet, one can determine the frequency-resolved radiation growth rate as a function of interaction length. However, varying the effective system length in this way has the additional complicating effect of introducing into the interaction a region of progressively decreasing axial field at the end of the region of uniform axial field. The consequences of this will be discussed in Sec. V.

III. THEORY

The theory for a free-electron laser operating in the collective regime, with an axial magnetic field larger than the gyroresonant value (Group II orbits) has been presented in detail elsewhere.[1,4-6] For the purpose of comparison with the radiation growth rate measurements presented later in this paper, we note that the linear growth rate is given by the solution of the dispersion equation[5]

$$(k+k_w-\kappa-\omega/v_\parallel)(k+k_w+\kappa-\omega/v_\parallel)(k-K_+)(k-K_-)$$

$$= \tfrac{1}{4}\beta_w^2\kappa^2\omega(\omega-\Omega_0-kv_\parallel)/\beta_\parallel c^2 \ , \qquad (1)$$

where $\beta_w \equiv v_w/v_\parallel$, $v_w \equiv \Omega_w v_\perp/(\Omega_0-k_w v_\parallel)$, $v_\parallel$ is the axial electron velocity, k_w ($\equiv 2\pi/\lambda_w$, where λ_w is the wiggler period) is the wiggler wavenumber, $\Omega_{0,w} \equiv |eB_{z,r}/\gamma mc|$, B_z and B_r denote the amplitudes of the axial and wiggler fields, $\gamma \equiv (1-v^2/c^2)^{-1/2}$ is the relativistic factor, (ω,k) represents the frequency and wavevector of the radiation, and

$$K_\pm \equiv \frac{1}{2v_\parallel}[\omega(1+\beta_\parallel)-\Omega_0] \pm \frac{1}{2}\left[\Delta K^2+2(\omega_b^2/\gamma c^2)(\Omega_0/\omega\beta_\parallel)\right]^{1/2} \ . \qquad (2)$$

In addition, $\omega_b \equiv (4\pi e^2 n_b/m)^{1/2}$ is the beam plasma frequency, n_b is the beam electron density, $\Delta K \equiv [\Omega_0-\omega(1-\beta_\parallel)]/v_\parallel$, $\beta_\parallel \equiv v_\parallel/c$, $\kappa^2 \equiv \omega_b^2\Phi/(\gamma\gamma_\parallel^2 v_\parallel^2)$, $\gamma_\parallel \equiv (1-v_\parallel^2/c^2)^{-1/2}$ and

$$\Phi \equiv 1-\beta_w^2\gamma_\parallel^2\Omega_0/[(1+\beta_w^2)\Omega_0-k_w v_\parallel] \ . \qquad (3)$$

The solutions to Eq. (1) have been discussed in detail in Freund, et al.[5] and will not be reproduced here.

We observe that $(v_w,v_\parallel)$ cannot be chosen arbitrarily. The energy conservation requirement implies that $v_\parallel^2+v_w^2=(1-\gamma^{-2})c^2$, which yields two distinct classes of solutions (see Fig. 2) corresponding to $\Omega_0<k_w v_\parallel$ (Group I) and $\Omega_0>k_w v_\parallel$ (Group II).[7] Since the parameters relevant to the observations described in this paper correspond to the Group II case, it is important to describe the characteristics of the interaction in this regime. In particular, we are concerned with the regime where

$$(1-\gamma_{\parallel}^2 v_w^2/c^2)\Omega_0 < k_w v_{\parallel} < \Omega_0, \tag{4}$$

for which $\Phi<0$. The dispersion equation (1) describes the coupling between the radiation and space-charge modes. In the absence of an axial magnetic field, $\Phi=1$ and the interaction proceeds via the coupling of a negative-energy space-charge wave and a positive-energy electromagnetic wave. However, in the regime described by Eq. (4), the space-charge waves have the dispersion relation $\omega=kv_{\parallel}\pm i|\kappa|v_{\parallel}$, and are intrinsically unstable for all wavevectors. A physical interpretation for this instability is given by Freund and Sprangle.[8] As a consequence, it might be expected that the wiggler-induced coupling between the electromagnetic and unstable electrostatic waves would result in an enhanced growth rate and interaction efficiency, since there is a uniform source of energy transfer from the beam to the space-charge modes. This expectation is indeed supported by experiments in which peak powers and efficiencies have been observed in this regime.[2,9]

Another consequence of this regime (4) relates to the phase relationship between the beam electrons and the ponderomotive wave. Although the experiment operates in the collective regime,[1] it is difficult to reduce Eq. (1) to a closed form expression for the gain when $\Phi<0$ (i.e., the regime of experimental interest in this paper), and we are forced to resort to numerical solutions of Eq. (1) in order to make detailed comparisons between theory and experiment. Therefore, we choose to illustrate the phase relationship by the expression for the small-signal, single particle (i.e., strong pump) gain[4]

$$G_L \simeq \frac{1}{8}\gamma_{\parallel}^2\beta_w^2(\kappa^2/k_w^2)(k_wL)^3\left[\frac{d}{dx}\left(\frac{\sin x}{x}\right)^2\right], \tag{5}$$

where G_L defines the amplification relative to the initial signal amplitude over a system of length L, and $x \equiv (\omega/v_\parallel - k - k_w)L/2$. It is clear that extrema occur for $x = \pm 1.3$ and when $\kappa^2 > 0$ peak amplification occurs for $x \simeq -1.3$. Thus, the phase velocity of the ponderomotive wave is $v_{ph} = \omega/(k+k_w) < v_\parallel$, and as the electrons lose energy to the wave they are decelerated. However, when $\kappa^2 < 0$ peak amplification occurs for $x \simeq 1.3$ which means that $v_{ph} > v_\parallel$; hence, the electrons undergo an "anomalous" increase in the axial velocity as they lose energy. In order to make this understandable, we observe that one consequence of the energy conservation relation is

$$\frac{dv_\parallel}{d\gamma} = \frac{c^2}{\gamma\gamma_\parallel^2 v_\parallel} \Phi \ , \tag{6}$$

which shows that when $\Phi < 0$ [see Eq. (4)], a decrease in energy results in an increase in axial velocity that is accompanied by a correspondingly greater decrease in the transverse velocity than occurs when $\Phi > 0$. The results of a particle simulation code[10] have also shown the axial electron velocity to increase as kinetic energy is lost.

Finally, it should be remarked that the theoretical work described here is based on a zero-temperature one-dimensional, ideal wiggler model in free space (i.e., waveguide geometry is not included). As a consequence, while the dispersion equation (1) can be expected to yield approximate values for the peak growth rate and bandwidth as long as the resonant frequency is far removed from any waveguide cutoffs, detailed spectra are not obtainable by this means. Fully self-consistent three-dimensional descriptions of millimeter-wave free-electron lasers including finite waveguide geometry have recently appeared in the literature[7,11];

however, because these theories are based upon thin annular beam models of the radial electron profile, they are not applicable to the present experiment.

IV. MEASUREMENTS OF RADIATION GROWTH

In order to perform measurements of radiation growth in a superradiant geometry, the length of the FEL interaction region is progressively increased during a sequence of experimental discharges by lengthening the solenoidal magnet that provides the axial magnetic field, while holding constant the amplitude of the axial field at the input to the wiggler magnet. Due to the large bore of the solenoidal magnet, proceeding in this fashion has the consequence that the axial magnetic field will fall off gradually towards the end of the interaction region, until the electrons are lost to the drift tube wall. This axial field end taper has consequences that will be considered in the next section. Note that the shape of the axial field end taper is nearly invariant with respect to the length of the solenoidal magnet, while the length of "uniform" interaction region prior to the end taper scales directly with magnet length. We therefore assume that so long as the electrons strike the wall still within the uniform section of the wiggler magnet, the effect of the end taper is approximately unchanged, and interpret the variation of the emission as the axial magnet is progressively lengthened as being primarily due to the increase in length of the uniform interaction region. [This interpretation is clearly somewhat suspect when nonlinear effects begin to become important.] This permits us to estimate the gain of the interaction in the uniform field region.

We have chosen to investigate the radiation growth for the experimental parameters that have produced the largest experimentally measured peak powers, that is γ =3.4, B_z=16 kG, B_r=1.4 kG. These conditions have produced a peak power that has been determined by direct calorimetric measurements to be $\gtrsim$ 75 MW at 6% experimental efficiency in a 15 nsec output pulse. A typical output radiation pulse is shown in Fig. 3, along with the voltage waveform of the electron beam diode. This peak power corresponds to the spectrum labeled "90 cm" in Fig. 4. The label "L" will be used to denote the axial position of the physical end of the solenoidal magnet, which is also the half-field point of the axial magnetic field, compared to the start of the wiggler entrance taper. Thus, L=90 cm corresponds to the case in which the axial field decreases to half of its uniform field value at a position 6 cm into the wiggler output taper. As will be discussed later, the electrons are actually lost in this case before reaching the wiggler output taper.

Figure 4 presents the FEL emission data at six frequencies in the range of 66 Ghz to 90 GHz as the length of the axial field magnet is progressively increased over a range of 36 cm, beginning at L=54 cm. (For still shorter magnet lengths, the radiation level could not be measured with the present experimental sensitivity). Each point corresponds to the peak emission during the 30 nsec flat portion of the accelerator voltage pulse, and is the average of data from at least three experimental discharges. The spectrum for L=54 cm is almost flat from 66 GHz to 80 GHz, but then drops by an order of magnitude at 85 GHz and 90 GHz. As the axial field magnet is lengthened by 6 cm and 12 cm (L=60 cm and 66 cm lines), the entire spectrum increases rapidly, while its shape remains approximately unchanged. The emission continues to grow as the axial

magnet is further lengthened (L=72 cm, 78 cm, and 90 cm), but the spectrum becomes strongly peaked near 75 GHz. Apparent evidence of the approach of saturation of the radiation growth process is appearing by L=90 cm. Based on the intersection of the uncoupled dispersion equations for the FEL interaction between the pump-shifted beam line and the electromagnetic waveguide modes, the interaction should couple to the TM_{01} mode of the drift tube at approximately 78 GHz for the parameters in the uniform portion of the interaction region.[1]

In order to better understand the process of radiation growth, as well as to facilitate comparisons with theoretical calculations, it is useful to reexamine the information implicit in Fig. 4 in several other formats. Figures 5 and 6 present the microwave radiation growth rate relative to the radiation level produced for L=54 cm. In Fig. 5, the radiation growth is followed at three frequencies, 66 GHz, 75 GHz, and 85 GHz, as the interaction length is progressively increased. It can be seen that for each frequency there is an interval of approximately exponential growth, followed by a roll-off in the growth rate. The roll-off occurs earliest and is largest at 85 GHz. For the first 18 cm of additional interaction length beyond that for L=54 cm, the growth is roughly comparable at 66 GHz and 75 GHz. The large peak at 75 GHz for L=90 cm appears to be more the result of the growth persisting longer at 75 GHz, while it rolls off prematurely at 66 GHz, than of an intrinsically higher growth rate at 75 GHz.

In Fig. 6, the cumulative radiation growth, relative to L=54 cm, is plotted for the six measured frequencies. At L=60 cm, the growth of the radiation has been fairly uniform over all of these frequencies. As the system is further lengthened the radiation growth develops less

uniformly. For instance, a dip in the growth develops at 80 GHz, so that there is slightly more cumulative radiation growth between L=54 cm and L=90 cm at 85 GHz, even through both the initial and final spectra show roughly an order of magnitude more radiation at 80 GHz than at 85 GHz. Until L=72 cm, the cumulative radiation growth has been comparable at 80 GHz, 85 GHz, and 90 GHz, but growth at 90 GHz begins to fall off as the system is further lengthened. In the lower frequency portion of the measured spectrum, growth is rapid at 66 GHz, but after L=72 cm, no further growth occurs. At 70 GHz, growth lags 66 GHz, but persists longer, so that the cumulative measured growth by L=90 cm is comparable. The growth at 75 GHz is comparable to that at 66 GHz until L=72 cm, but persists as the interaction region is further lengthened, resulting in the large peak seen at this frequency at L=90 cm. Thus, the experimentally observed radiation growth in the frequency range from 65 GHz to 90 GHz is significantly more complicated than might be expected if one assumed simply that a broadband instability with a well-defined frequency-dependent growth rate had progressively amplified spontaneous emission to produce the final highly peaked spectrum.

Figure 7 treats each additional 6 cm length of the interaction region as a section of an FEL amplifier, and presents the growth rate (gain), in dB/cm, attributed to that increment in length. The linear growth rate is one of the quantities that FEL theory can directly calculate in order to compare with the experimental measurements. Theory would suggest that the growth rate should remain high and be relatively constant until nonlinear effects become important and cause the gain to roll off. The highest experimentally measured growth rates are observed when the interaction length is at its shortest. Between L=54 cm and L=60 cm, the growth rate

at all six measured frequencies is in the range of 1.4 to 1.8 dB/cm. The linear theory using the model discussed previously in Sec. III predicts [Eq. (1)] that the maximum of the frequency-dependent growth rate is $Im(k)/k_w = 0.128$, or 2.3 dB/cm. The agreement between this calculation and the experiment is remarkably good, considering the incomplete nature of the one-dimensional theoretical model, which uses an ideal wiggler, and a zero-temperature beam, and which does not include waveguide effects. The omission of waveguide effects causes the model to predict this peak growth rate to occur at 95 GHz, a higher frequency than that at which it is experimentally observed. The expected FEL coupling frequency is approximately

$$\omega=\beta_{\parallel}(1+\beta_{\parallel})\gamma_{\parallel}^2 k_w c \tag{7}$$

for a one-dimensional free-space model. When waveguide effects are included, this frequency is reduced, and we find that resonance is shifted to

$$\omega=\gamma_{\parallel}^2 k_w v_{\parallel}\left(1\pm[\beta_{\parallel}^2-\omega_{co}^2/(\gamma_z^2 k_w^2 c^2)]^{1/2}\right) \tag{8}$$

where ω_{co} is the cutoff frequency of the particular waveguide mode of interest.[1] The broad bandwidth of the growth rate observed here is also consistent with theoretical predictions for an FEL operating above gyroresonance on Group II trajectories, where a very broadband instability is predicted.[5] In fact, numerical solution of Eq. (1) suggests that the linear growth rate predicted by one-dimensional theory should dip by less than 10% over more than a full octave of instantaneous bandwidth, from

52.5 GHz to 112.5 GHz. This suggests that the predicted voltage gain-bandwidth product of a 30 dB linear amplifier would be approximately 3.1×10^{12} Hz.

The second growth rate measurement is shown for the interval L=66 cm to L=72 cm. At this point in the interaction, the growth rate has become strongly peaked near 75 GHz at a value of about 1.6 dB/cm, with a secondary maximum near 66 GHz. The growth rates at the higher frequencies, in particular, have fallen off dramatically. The last measured interval, from L=78 cm to L=90 cm, shows uniformly low growth rates at all frequencies, suggesting that the interaction is near saturation.

One usual measure of the width of the emission peaks of Fig. 4 is the half-power spectral bandwidth., However, this quantity is not easily determined for the curves at L=54 cm, 60 cm, and 66 cm, since they are very broad and flat. The next three curves, at L=72 cm, 78 cm, and 90 cm, would each produce an estimate of ~3 GHz for the half-power spectral bandwidth, but it is difficult to determine the value more precisely, since the data points are at approximately 5 GHz intervals. For that reason, we have chosen to demonstrate the progressive narrowing of the emission spectrum in Fig. 8 by the ratio of the emission at 75 GHz to the average of the emission at the two adjacent measured frequencies, which presents one measure of the sharpness of the spectral peak at 75 GHz. This ratio is near unity until L=66 cm. The ratio rises rapidly thereafter, reaching a value of about 14 by L=78 cm. This may be interpreted as "growth narrowing" of the emission spectrum. By L=90 cm, the emission has become slightly less peaked at 75 GHz, perhaps due to saturation effects flattening the emission spectrum. As discussed above,

the information in Figs. 5 to 7 suggests that nonlinear effects, rather than progressive narrowing due simply to a finite linear growth bandwidth, are responsible for the measured emission bandwidths for the longer interaction length cases, i.e. L=72 cm, 78 cm, and 90 cm.

V. EFFECTS OF AN AXIAL FIELD END TAPER

The introduction of an axial field end taper is a side effect of the means used experimentally to vary the effective length of the FEL interaction region, as is discussed in the preceding sections of this paper. We reiterate that each measured interaction length ends with such an axial field end taper, whose macroscopic characteristics, namely a particular rate of fall of B_z at constant B_r, leading to loss of the electrons to the drift tube wall, are identical. We therefore have interpreted the progressive growth of the emission spectrum as the axial magnet is lengthened as due to the progressive lengthening of the uniform interaction region that precedes the axial field end taper. In this section, we consider more closely the effects of this axial field end taper. We point out that it is a complex region, whose effects are not fully understood, and that it can have important experimental consequences. In particular, for the parameters being discussed in this paper, the introduction of an axial field taper at the end of the uniform interaction region (that is, the L=90 cm case discussed in the previous section of this paper) results in a large increase in the measured millimeter-wave radiation produced by the FEL interaction, and therefore in the experimental efficiency of the interaction, compared to the case in which the axial field is held constant throughout the interaction

region. This effect had been reported previously,[1] but in this section it is studied in greater detail.

Figure 9 shows a comparison of the emission spectrum produced by the FEL with an axial field end taper (due to ending the axial field magnet at L=90 cm) with the emission spectrum for the case of uniform B_z (which is produced by extending the axial field magnet well beyond the end of the wiggler magnet). It is clear that the line labeled "tapered B_z" shows substantially larger emission, particularly near 75 GHz, than the line of "uniform B_z". These spectra are similar to those published previously,[1] but are results from a new set of data that was taken in conjunction with the data presented in the previous section of this paper. In addition to the increase in emission, there is some evidence of a shift to lower frequencies compared to the uniform B_z spectrum, as was also reported previously. The pyroelectric detector data also suggest an approximate doubling in power and efficiency between these two cases.

Additional evidence of the large increase in power that is due to the axial field end taper is shown in Fig. 10, which shows the results of open shutter photography of full atmospheric pressure microwave-produced air breakdown plasmas.[12] These plasmas are produced by focusing the FEL emission into ambient laboratory air using a 11.5 cm focal length, f/0.25 parabolic mirror. (The mirror is positioned to the right, in each half of the figure.) Air breakdown will occur in the vicinity of the mirror focus, wherever the microwave electric field exceeds the threshold for air breakdown. This threshold is estimated to lie in the range 3.3 MW/cm^2 [13] to 4.5 MW/cm^2 [14] for a 15 nsec radiation pulse. It is clear that the front cross section of the breakdown has increased by more than a factor of two for the breakdown plasma resulting from the system with a

tapered B_z, compared to the uniform B_z case, suggesting a comparable increase in the emission.

Finally, direct calorimetric measurement of the energy in the 15 nsec microwave pulse demonstrates peak powers exceeding 75 MW with the axial field end taper. The best comparable shot with no end taper corresponded to 35 MW.

Figures 11 through 14 describe some of the parametric variation, as a function of axial position in the interaction region, that is predicted to result when the end of the axial field magnet occurs before the end of the wiggler magnet. Figure 11 shows the normalized axial and wiggler fields used for the chosen example, in which L=80 cm. The curve labeled B_r shows the entry taper into the wiggler, the uniform wiggler region, and the exit taper that is used to bring the electrons out of the interaction region adiabatically, provided B_z remains uniform. The curve labeled B_z shows the axial magnetic field for the case of L=80 cm. (For other positions of the end of the axial field magnet, the entire curve labeled B_z would be translated left or right, with the value of B_z held constant at z=0 cm.)

In the absence of a wiggler magnetic field, the gradual decrease of the axial magnetic field would slowly send the magnetized electron beam (initial radius, r=3 mm) into the drift tube wall at r=5.4 mm. However, in the presence of a helical wiggler, and for an axial magnetic field value above gyroresonance, as is the case here, the decreasing value of B_z is predicted to have a more drastic effect, as shown in Fig. 12. (See Fig. 2 and observe that the transverse electron energy and, hence, the radius of the electron orbits, increases with decreasing B_z for Group II orbits.) Figure 12 is a plot of results from a single-particle trajectory code that injects an electron along B_z at a particular initial radius, and

follows its orbit in the combination of B_z and the full three-dimensional fields due to the wiggler magnet. The code has been used to follow electrons launched at r=0 and at r=2.8 mm through the wiggler entrance taper at uniform axial field, the region of both uniform wiggler and uniform axial magnetic fields, and then through the axial field end taper at constant wiggler magnetic field which is produced by ending the axial field magnet at L=80 cm. Note that the axial field end taper is modeled in the code simply as a falling value of axial B_z rather than by the divergence of magnetic field lines that actually occurs near the end of the solenoidal magnet; this is a reasonable approximation in this case, since the electrons are sent to the wall by the approach to gyroresonance caused by the decreasing axial field much more rapidly than by the divergence of field lines. Note also that the code does not include space-charge effects. In fact, as the electrons gain kinetic energy by approaching the walls, this drives them towards gyroresonance even more rapidly. It is clear from Fig. 12 that the effects of the end of the axial field magnet are felt several tens of centimeters upstream from the physical end of the magnet. In addition, in this simulation, all the electrons are driven to the drift tube wall before reaching the half-field point at L=80 cm.

Figure 13 follows an electron launched at an initial radius of zero, and plots the calculated axial velocity ($\beta_{\parallel}$) and transverse velocity ($\beta_{\perp}$) as a function of axial position. The transverse velocity begins to increase perceptibly several tens of centimeters from the magnet end, and increases rapidly beginning about 20 cm from the magnet end. This increase in transverse velocity should increase the strength of the FEL interaction. (However, it also results in an increased axial velocity

spread which may have deleterious effects.) At the same time, the axial velocity falls off, resulting in a shift of the gain to lower frequencies.

The latter effect is shown in Fig. 14, which plots the calculated frequencies [via Eq. 8)] of the FEL coupling to the TE_{11} and TM_{01} modes of the drift tube for the axial electron velocities shown in Fig. 13. Note that the linear gain is expected to be very broad band, and this figure simply predicts the frequency of strongest growth for each of these modes. As $\beta_{\parallel}$ drops due to the approach to the magnet end at L=80 cm, the frequency of the TM_{01} mode drops rapidly, until the calculated coupling vanishes at about 55 GHz near z=55 cm. The TE_{11} mode drops more gradually from an initial coupling frequency of about 95 GHz. It passes through 75 GHz near z=55 cm, and falls rapidly thereafter.

It is evident from the foregoing analysis that the effects of the axial field end taper extend over several tens of centimeters. Given the growth rates inferred in the previous section of this paper, a region of this extent is clearly long enough to strongly affect the emission spectrum, as is seen experimentally in Fig. 9.

It is clear that one general effect should be to shift the growth to lower frequencies, and this effect is in fact observed in Fig. 9. However, it is not self-evident that the overall effect will be to increase the power and efficiency of the interaction and to narrow the emission linewidth, as is also observed in this case. In fact, the axial field end taper has a kinematic effect that is opposite from that produced in the usual tapered wiggler experiment, in which either the wiggler amplitude or period is adjusted to compensate for the reduced axial electron velocity caused by the extraction of kinetic energy from the electron beam into the radiation field. The axial field end taper in fact

reduces the axial electron velocity, by converting axial kinetic energy to transverse motion. However, as pointed out in Sec. III, this is in fact the correct sense of axial field taper to compensate for the anomalous axial acceleration that electrons experience in this parameter range as kinetic energy is extracted from the beam. Thus, the increase in power and efficiency that is measured in this case may in fact be due to tapering the FEL interaction parameters in such a way as to compensate for energy extraction from the electron beam. Successful tapered wiggler experiments have previously been reported at much shorter wavelengths for Compton FEL's operating in the trapped particle regime.[15,16]

As stated in the previous section, the narrowing of the emission spectrum observed as the interaction length is increased beyond the L=66 cm case appears to be due primarily to nonlinear effects in a system approaching saturation, rather than linear growth narrowing. The narrower emission spectrum seen in Fig. 9 for the system with "tapered B_z" compared to "uniform B_z" appears due mostly to the loss of higher frequency gain shown by the shift to lower frequencies evident in Fig. 14 as the axial field taper reduces axial velocity. As seen in Fig. 5, some high frequency gain appears to take place even at long interaction lengths, so that the loss of some uniform interaction region due to the axial field end taper may cause the reduction in higher frequency emission, and thus the spectral narrowing, while simultaneously enhancing the lower frequencies.

It should be emphasized that the case labeled "uniform B_z," corresponding to B_z=16 kG and B_r=1.4 kG, was experimentally determined to be the optimum experimental wiggler field at this value of axial magnetic field. In other words, varying the gain by changing the wiggler field at this value of B_z is found experimentally to reduce the final emission

amplitude. Thus, it does not appear likely that the increased emission that results from ending the axial field magnet at L=90 cm is due to the interaction region for the uniform field case having initially been too long at these parameters, and radiation reabsorption having taken place. If that were the case, varying the gain instead of the interaction length should have a similar favorable effect on the emission amplitude. Experimentally, it does not. Furthermore, the experimental trend at lower values of uniform B_z, with B_r separately optimized in each case, is to lower measured output powers.

VI. CONCLUSIONS

In summary, a set of measurements have been performed to determine the radiation growth rate in a high power superradiant FEL amplifier operating in the collective regime. This study was carried out by varying the effective length of the interaction region by changing the length of the magnet producing the axial magnetic field. The change in emission spectrum as a function of interaction length permits the experimental determination of frequency-resolved growth rates, as well as the observation of such effects as spectral narrowing and saturation. Using this procedure, large radiation growth rates have been observed, in the range of 1.4 to 1.8 dB/cm, over the range from 65 GHz to 90 GHz. These growth rates are in good agreement with predictions of theory.

A side effect of the method used to vary the effective interaction length is the introduction into the experiment of a region of uniform wiggler magnetic field and downward tapering axial magnetic field. While this effect complicates the interpretation of the radiation growth rate data, it is separately interesting. It is experimentally observed that

the presence of this axial field and taper can strongly enhance the overall power and efficiency of the interaction, increasing the experimental power to $\gtrsim$ 75 MW at 6% efficiency. Since the axial field taper is of the correct sense to compensate for axial electron velocity changes due to extraction of kinetic energy from the electron beam into the radiation field, a possible interpretation of this effect is as a "tapered interaction" FEL, similar to the tapered wiggler FEL's that are being investigated to improve the efficiency at shorter wavelengths.

ACKNOWLEDGMENTS

We acknowledge the expert technical assistance provided by D. Hardesty. This research was supported by the Naval Sea Systems Command under Contract No. SF68-342.

References

1. S.H. Gold, W.M. Black, H.P. Freund, V.L. Granatstein, R.H. Jackson, P.C. Efthimion, and A.K. Kinkead, Phys. Fluids 26, 2683 (1983).

2. R.H. Jackson, S.H. Gold, R.K. Parker, H.P. Freund, P.C. Efthimion, V.L. Granatstein, M. Herndon, A.K. Kinkead, J.E. Kosakowski, and T.J.T. Kwan, IEEE J. Quantum Electron. *QE*-19, 346 (1983).

3. J.A. Pasour and S.P. Schlesinger, Rev. Sci. Instrum. 48, 1355 (1977).

4. H.P. Freund, P. Sprangle, D. Dillenburg, E.H. da Jornada, B. Liberman, and R.S. Schneider, Phys. Rev. A24, 1965 (1981).

5. H.P. Freund, P. Sprangle, D. Dillenburg, E.H. da Jornada, R.S. Schneider, and B. Liberman, Phys. Rev. A26, 2004 (1982).

6. L. Friedland and A. Fruchtman, Phys Rev. A25, 2693 (1982).

7. H.P. Freund, S. Johnston, and P. Sprangle, IEEE J. Quantum Electron. *QE*−19, 322 (1983).

9. S.H. Gold, R.H. Jackson, R.K. Parker, H.P. Freund, V.L. Granatstein, P.C. Efthimion, M. Herndon, and A.K. Kinkead, "Free-electron generators of coherent radiation," based on lectures of the Office of Naval Research Sponsored Workshop, June 22-25, 1981, Sun Valley, Idaho, in *Physics of Quantum Electronics, Vol. 9*, edited by S.F. Jacobs, et al. [Addison-Wesley, Reading, 1982], p. 741.

10. H.P. Freund, Phys. Rev. A27, 1977 (1983).

11. H.P. Freund and A.K. Ganguly, "3-Dimensional Theory of the Free-Electron Laser in the Collective Regime," Phys. Rev. A—General Physics, V28, N6, 3438-3449, Dec. 1983.

12. S.H. Gold, W.M. Black, V.L. Granatstein, and A.K. Kinkead, Appl. Phys. Lett., to be published.

13. A.W. Ali, private communication.

14. P. Felsenthal and J.M. Proud, Phys. Rev. 139, A1796 (1965).

15. R.W. Warren, B.E. Newnam, J.G. Winston, W.E. Stein, L.M. Young, and C.A. Brau, IEEE J. Quantum Electron *QE*−19, 391 (1983).

16. J.M. Slater, J.L. Adamski, D.C. Quimby, T.L. Churchill, L.Y. Nelson, and R.E. Center, IEEE J. Quantum Electron. *QE*−19, 374 (1983).

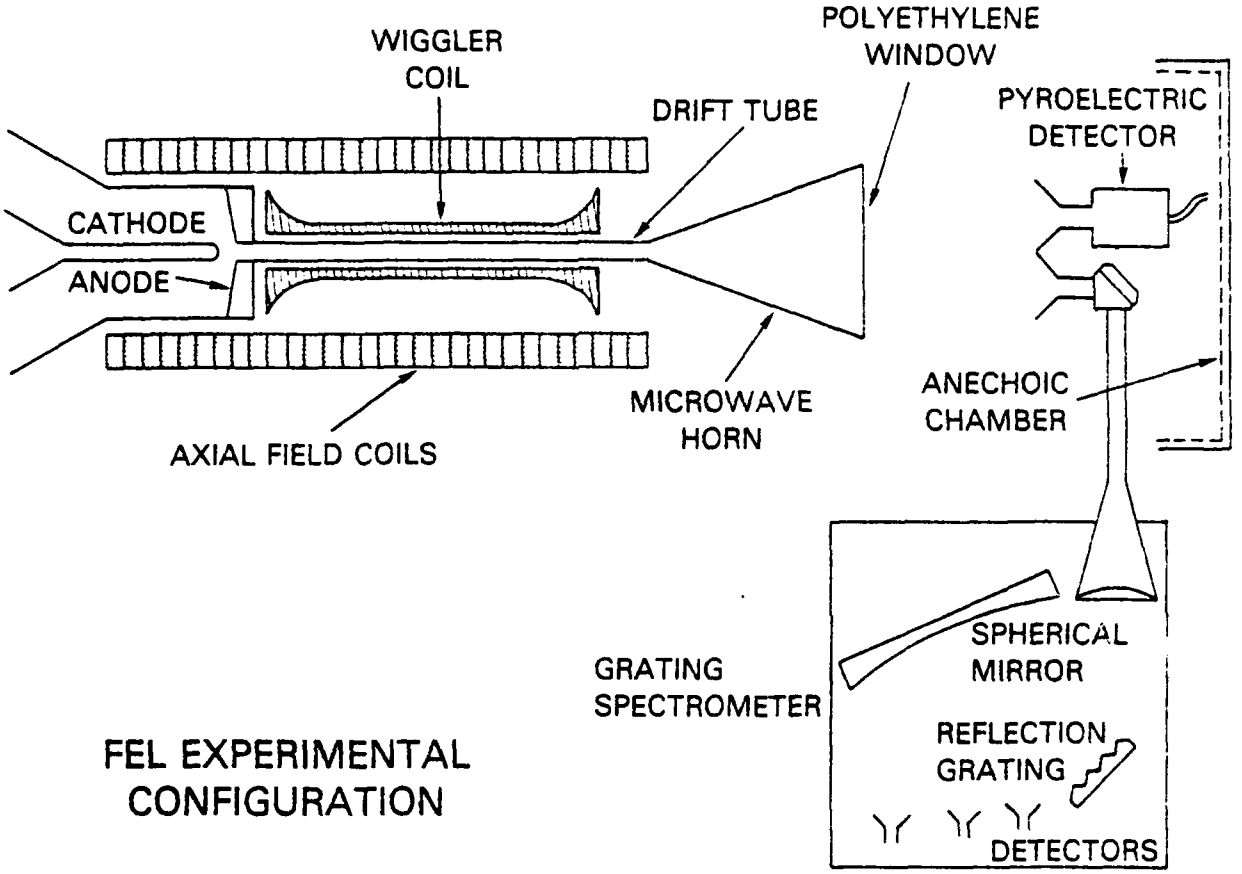

Fig. 1. Diagram of the free-electron laser experimental configuration, showing the setup used to perform frequency-resolved measurements.

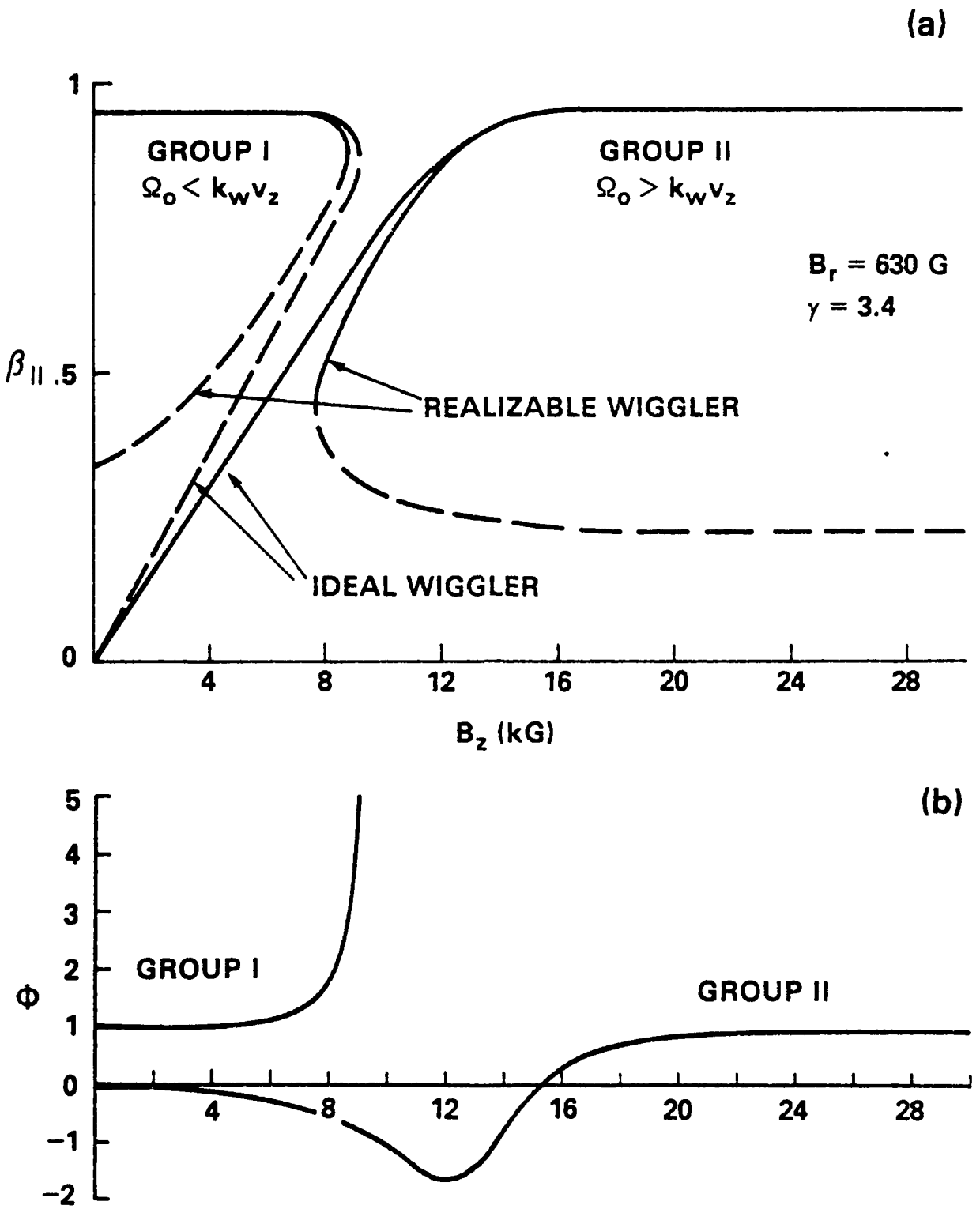

Fig. 2. Plots of (a) $\beta_{\parallel}$ and (b) ϕ versus axial guide field for B_r=630 G, γ=3.4. The axial velocity is shown for both ideal and realizable wigglers. The dashed lines describe unstable orbits. Here ϕ is calculated for an ideal wiggler.

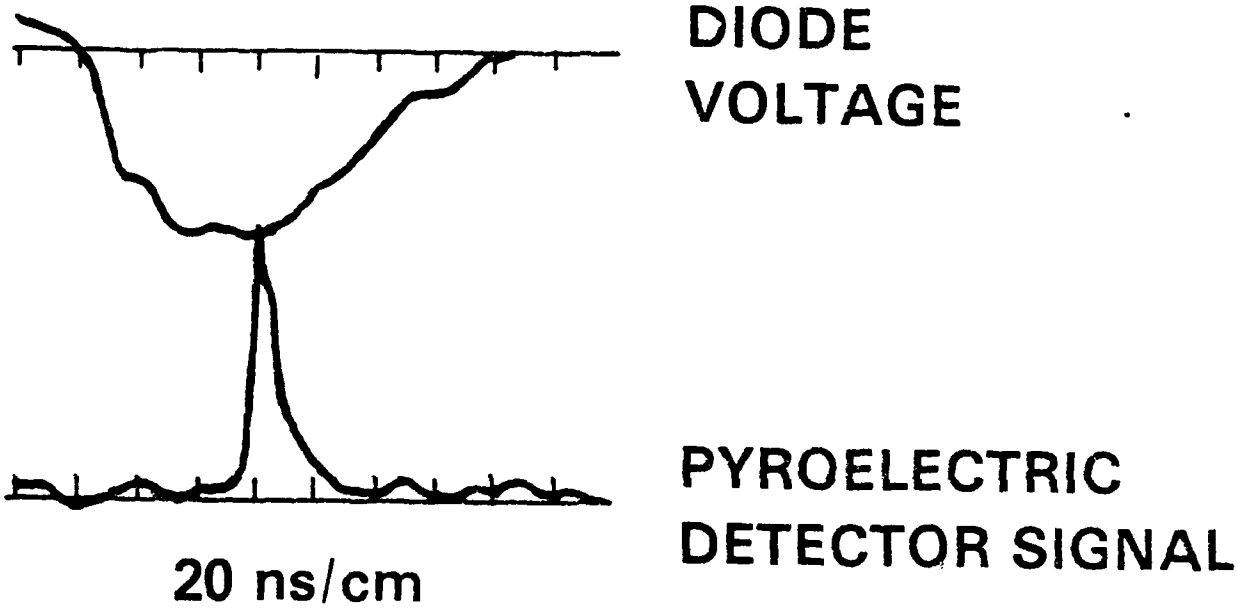

Fig. 3. Typical diode voltage pulse and microwave radiation pulse versus time.

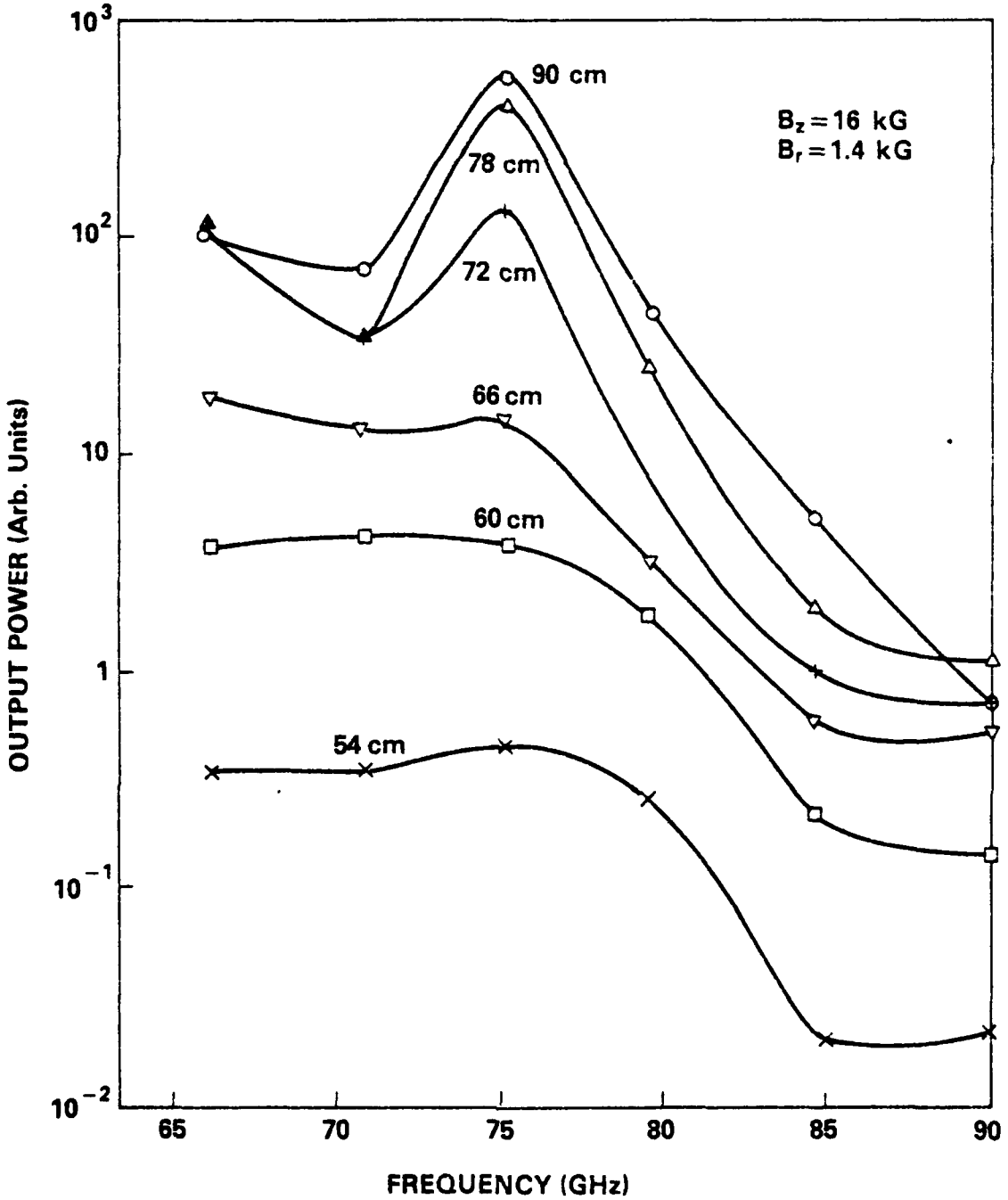

Fig. 4. Growth of the FEL emission spectrum at B_z=16 kG, B_r=1.4 kG for six frequencies between 66 GHz and 90 GHz as a function of the position (L) of the end of the axial field magnet with respect to the start of the wiggler magnet.

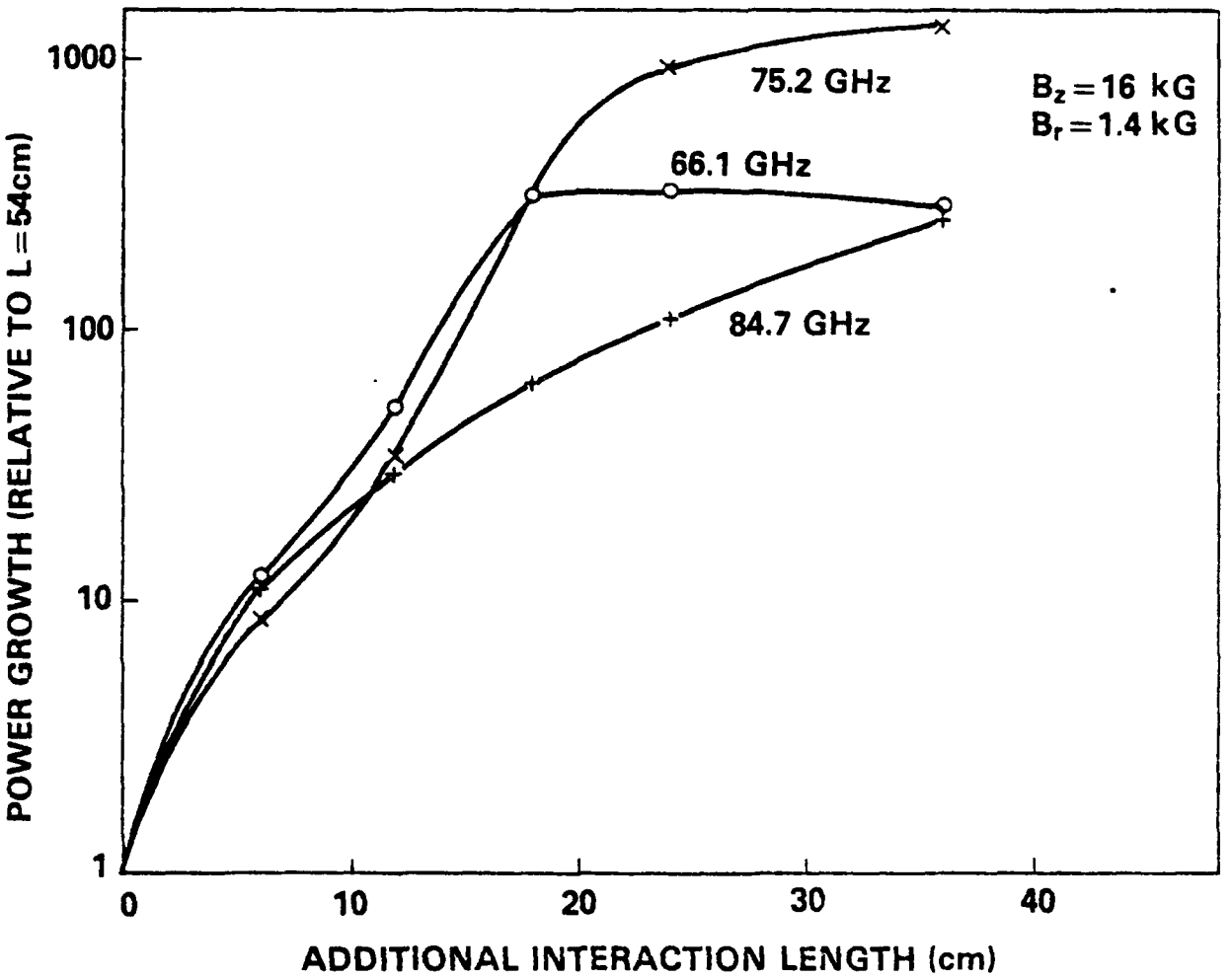

Fig. 5. FEL radiation growth at 66.1 GHz, 75.2 GHz, and 84.6 GHz relative to L=54 cm.

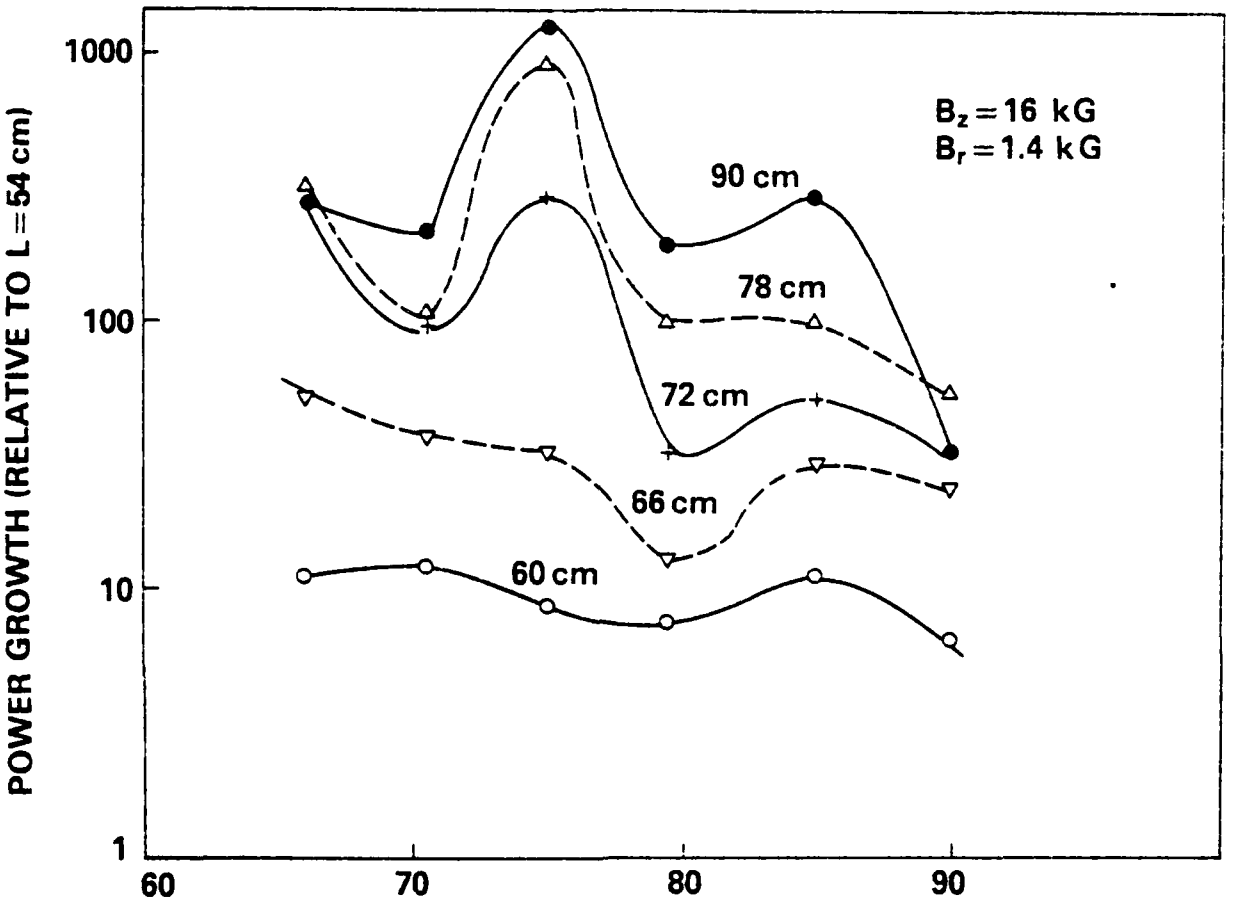

Fig. 6. FEL radiation growth between 66 GHz and 90 GHz relative to L=54 cm.

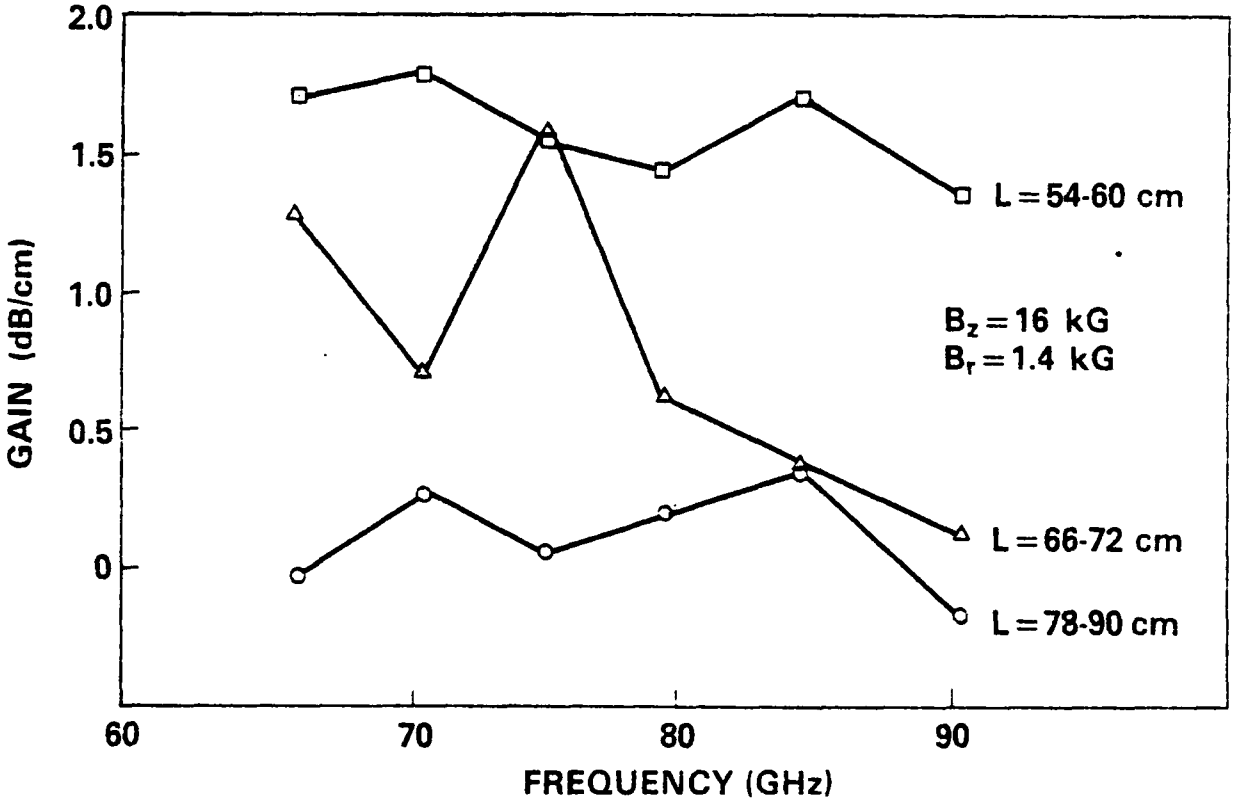

Fig. 7. Growth rate of the FEL emission spectrum over three intervals, L=54-60 cm, L=66-72 cm, and L=78-90 cm.

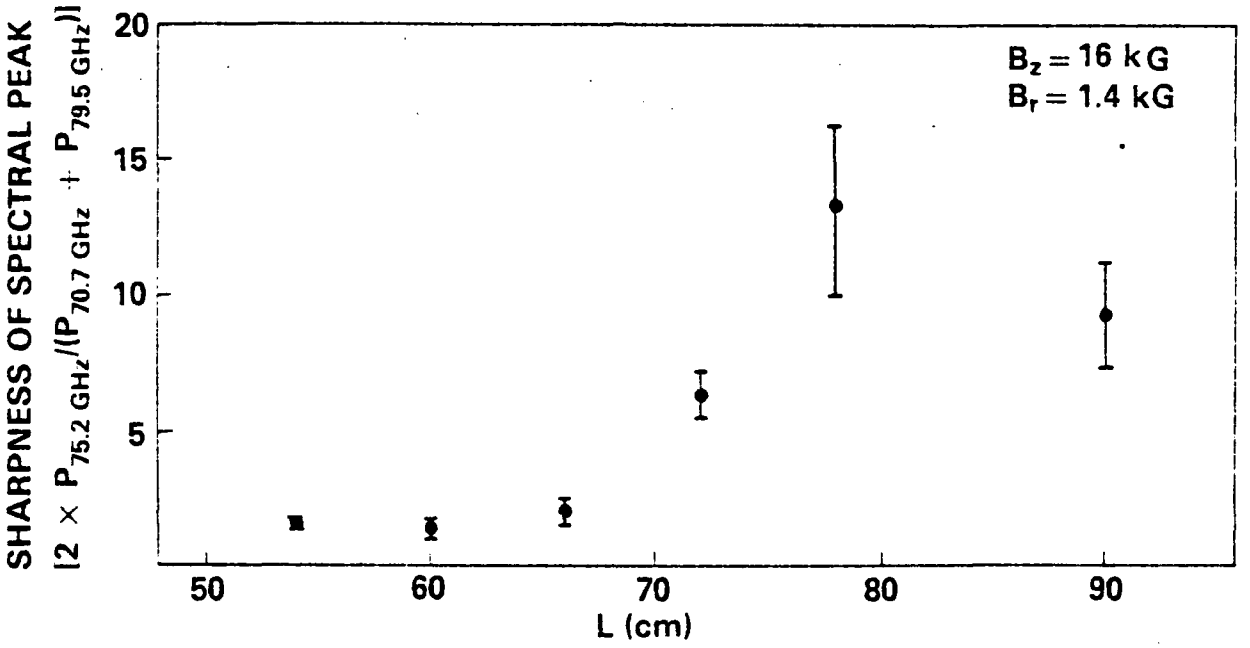

Fig. 8. FEL spectral narrowing as a function of interaction length. Ratio of emission at 75.2 GHz to the average of the emission measured at 70.7 GHz and 79.5 GHz.

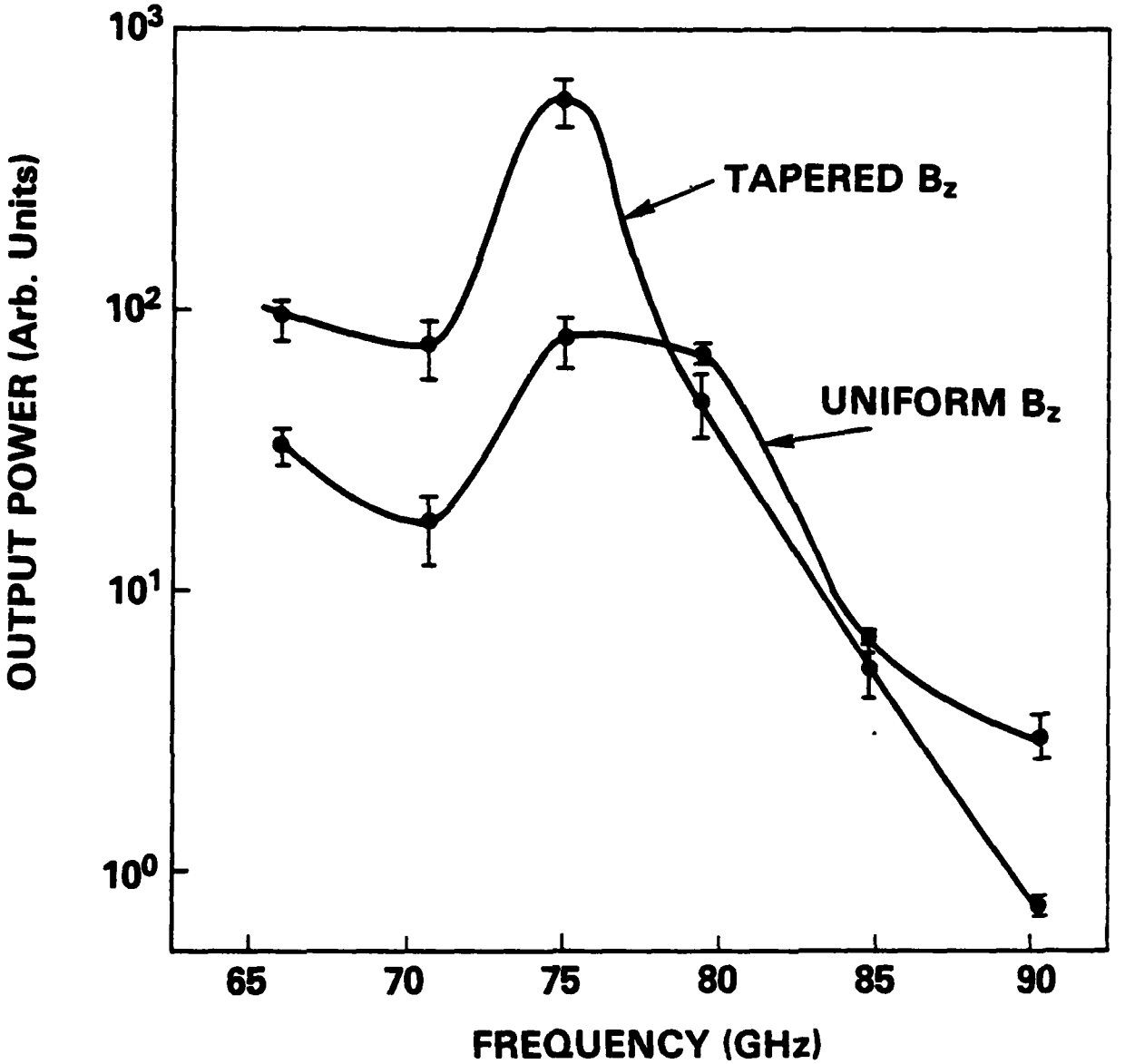

Fig. 9. Magnet shortening experiment. Comparison of the emission spectrum at B_z=16 kG, B_r=1.4 kG, for the case with an axial field end taper to the emission spectrum for the case of uniform B_z.

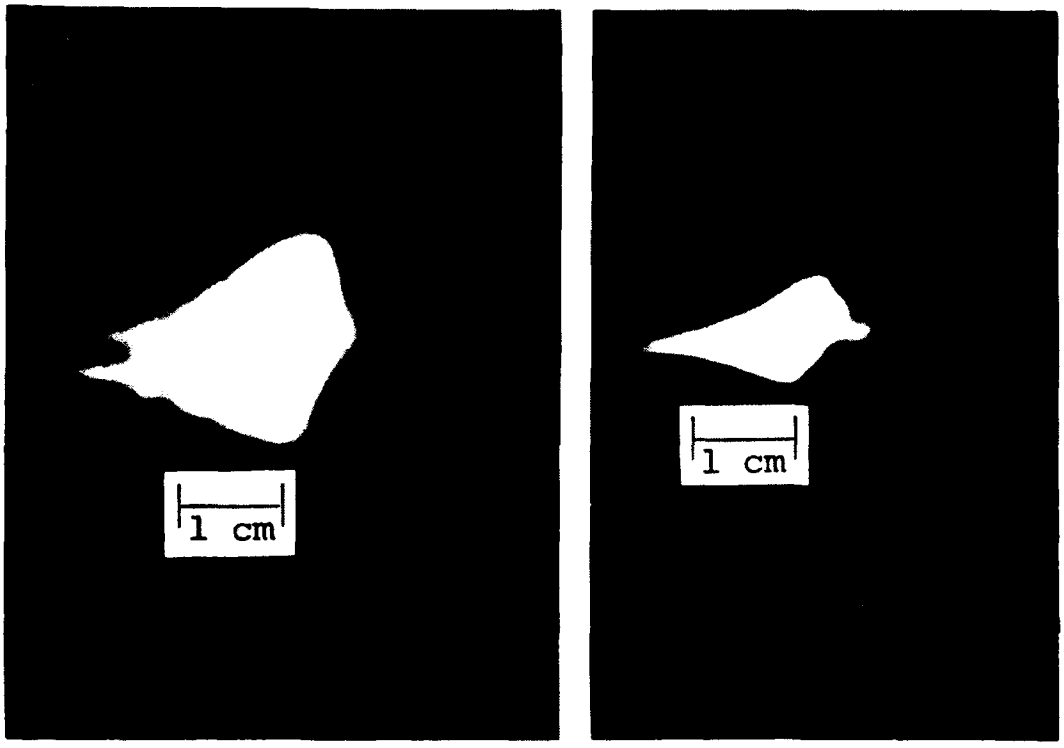

Fig. 10. Atmospheric pressure microwave-produced air breakdown focal patterns for the case of "tapered B_z" (left) and "uniform B_z" (right).

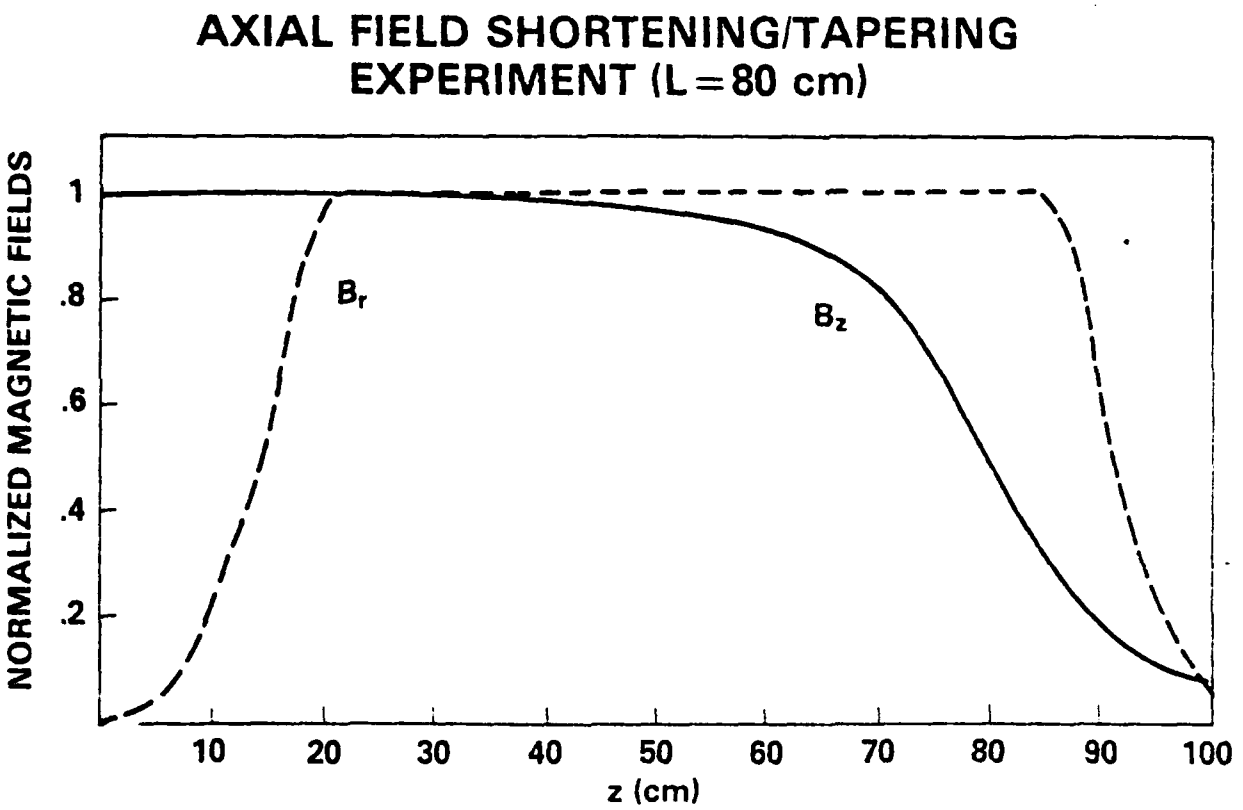

Fig. 11. Axial and wiggler magnetic field profiles for L=80 cm.

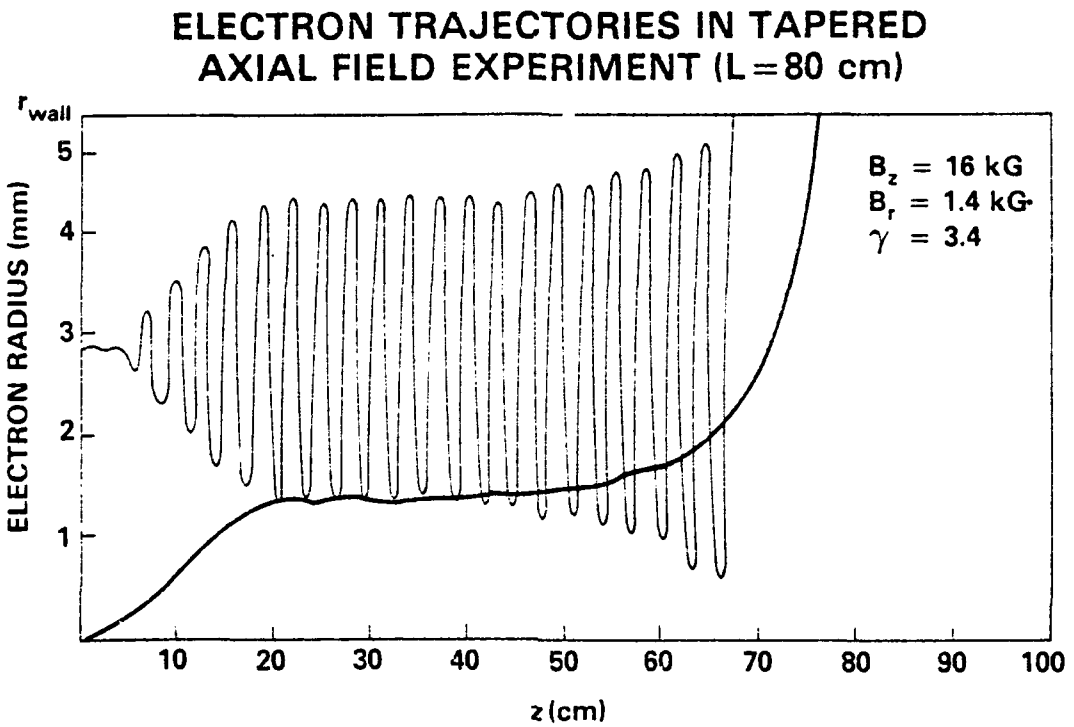

Fig. 12. Electron trajectories in the combined axial and wiggler magnetic fields for L=80 cm. Trajectories originating on axis and near the beam edge are shown.

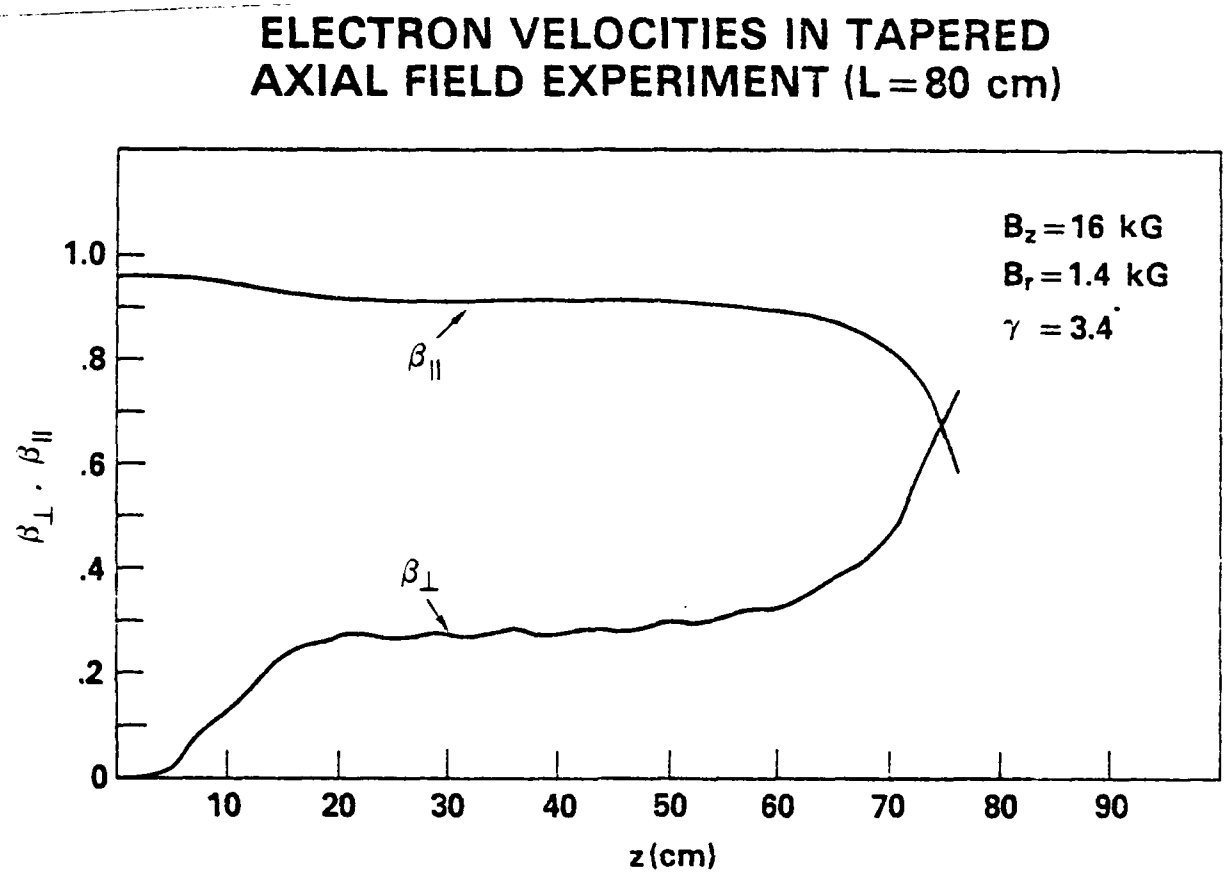

Fig. 13. Electron velocities in the combined axial and wiggler magnetic fields for L=80 cm.

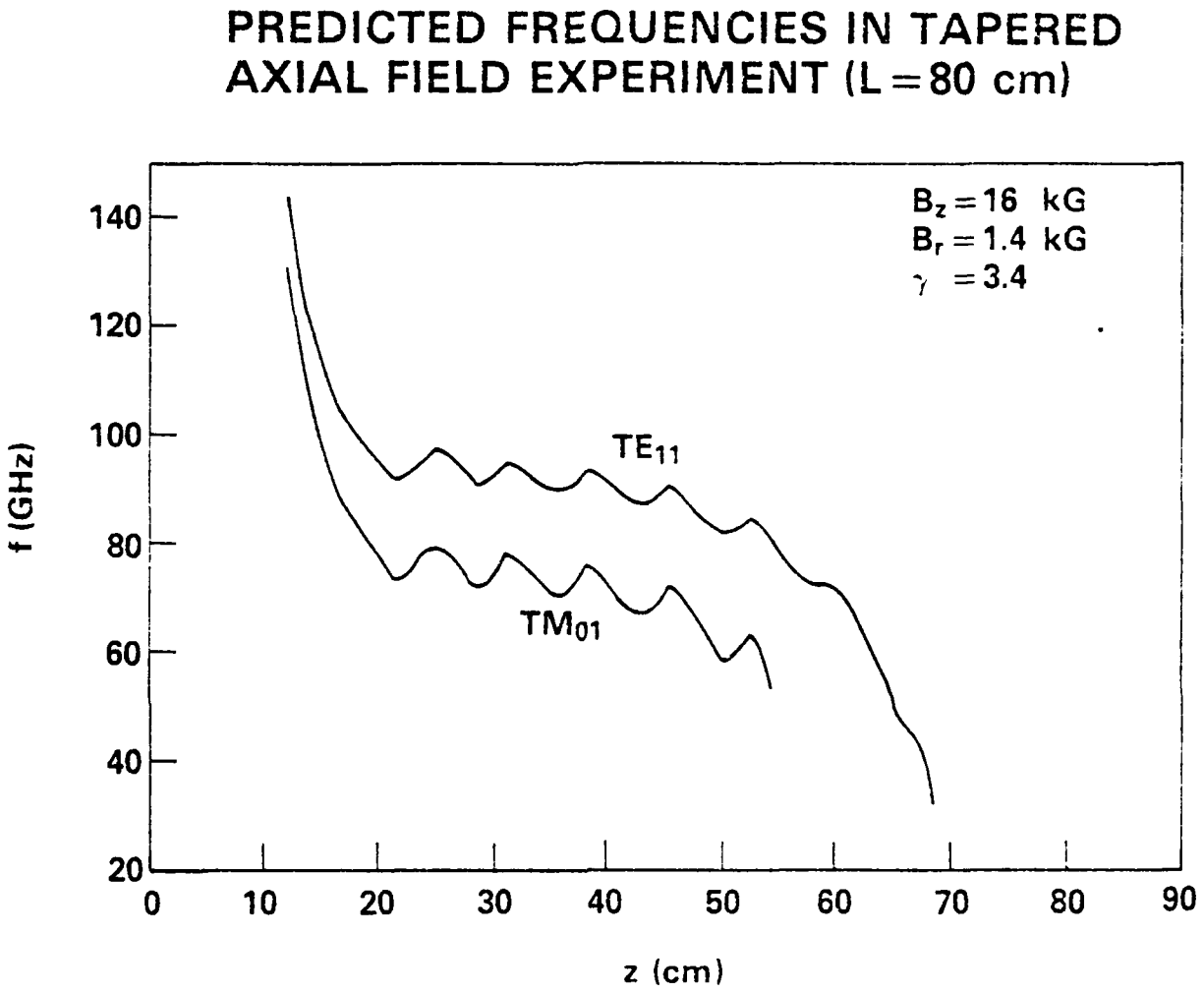

Fig. 14. Predicted FEL coupling frequencies as a function of axial position for L=80 cm.

END

FILMED

5-84

DTIC